Discovery of a Temperature-Dependent Upflow in the Plage Region during a Gradual Phase of the X-Class Flare

Shinsuke IMADA, Hirohisa HARA, Tetsuya WATANABE, and Suguru KAMIO

National Astronomical Observatory of Japan, 2-21-1 Osawa, Mitaka, Tokyo 181-8588

shinsuke.imada@nao.ac.jp

Ayumi ASAI

Nobeyama Solar Radio Observatory, Minamisaku, Nagano 384-1305

Keiichi MATSUZAKI

Institute of Space and Astronautical Science, Japan Aerospace Exploration Agency, Kanagawa,

3-1-1 Yoshinodai, Sagamihara, Kanagawa 229-8510

Louise K. HARRA

UCL-Mullard Space Science Laboratory, Holmbury St Mary, Dorking, Surrey, RH5 6NT, UK

and

John T. MARISKA

Space Science Division, Naval Research Laboratory, Washington DC 20375, USA

Abstract

We present Hinode/EIS raster scan observations of the plage region taken during the gradual phase of the GOES X3.2 flare that occurred on 2006 December 13. The plage region is located $200''$ east of the flare arcade. The plage region has a small transient coronal hole. The transient coronal hole is strongly affected by an X-class flare, and upflows are observed at its boundary. Multi-wavelength spectral observations allow us to determine velocities from the Doppler shifts at different temperatures. Strong upflows along with stationary plasma have been observed in the Fe XV line 284.2 Å ($\log T/\mathrm{K} = 6.3$) in the plage region. The strong upflows reach almost $150\,\mathrm{km\,s^{-1}}$, which was estimated by a two-component Gaussian fitting. On the other hand, at a lower corona/transition region temperature (He II, 256.3 Å, $\log T/\mathrm{K} = 4.9$), very weak upflows, almost stationary, have been observed. We find that these upflow velocities clearly depend on the temperature with the hottest line, Fe XV, showing the fastest upflow velocity and the second-highest line, Fe XIV, showing the second-highest upflow velocity ($130\,\mathrm{km\,s^{-1}}$). All velocities are below the sound speed. The trend of the upflow dependence on temperature dramatically changes at 1 MK. These results suggest that heating may have an important role for strong upflow.

Key words: Sun: corona — Sun: coronal mass ejection — Sun: flares — Sun: solar wind

1. Introduction

One of major aspects of solar flares is the rapid energy conversion of stored free magnetic energy in corona to thermal energy, kinetic energy or non-thermal particle energy. These energy conversions are fundamental and essential to understand the dynamical behavior of the solar corona. Over the several decades, considerable effort has been devoted toward understanding the physical mechanism of solar flares, and various models have been proposed (e.g., Chen & Shibata 2000). One of the popular mechanisms of a solar flare is magnetic reconnection, because magnetic field energy can be rapidly released to plasma energy. Various features expected from the magnetic reconnection model have been confirmed by modern observations. These include a cusp-like structure in X-ray images (e.g., Tsuneta et al. 1992), non-thermal electron acceleration (e.g., Masuda et al. 1994), chromospheric evaporation (e.g., Teriaca et al. 2003), reconnection inflow and outflows (e.g., Yokoyama et al. 2001), and plasmoid ejection (e.g., Ohyama & Shibata 1998).

Another aspect of solar flares is their impact on their surroundings—larger-scale magnetic reconfigurations can

occur following a flare. The reconfiguration of a magnetic field may cause a topological change from a closed magnetic field line to a magnetic field line (e.g., Crooker et al. 2002). This topology change forms transient coronal holes. Transient coronal holes are regions of low-density plasma, located in open magnetic field regions where the magnetic field lines connect the solar surface directly to interplanetary space. These open-field configurations efficiently transport upflowing plasma and form the solar wind. Attrill et al. (2006) discussed changes in the magnetic field topology associated with coronal mass ejection (CME). According to their scenario, the magnetic loops of the CME expand, and eventually push against the oppositely oriented open magnetic field of the polar coronal hole. This condition causes successive magnetic reconnection, and some parts of the magnetic loop topology change from closed to open.

In this paper, we focus on the behavior of the plage region during a gradual phase of the GOES X3.2 flare on 2006 December 13 using the EUV Imaging Spectrometer (EIS)/Hinode. The flare took place at 02:14 UT on NOAA 10930, which was the third of four GOES X-class flares in the time period from December 5 to 15. Some typical features

were observed by many solar telescopes, such as an X-ray wave, an EIT wave, white light enhancement, and a CME with this flare. Our motivation of this work is to understand the formation of upflow from the open magnetic field lines associated with an X-class flare using EIS observations. We believe that this study can contribute to our understanding of solar-wind formation.

2. Observations and Data Analysis

The Hinode spacecraft was launched on 2006 September 22 UT (Kosugi et al. 2007). It is a Japanese mission collaborating with US and UK with three instruments on-board: the Solar Optical Telescope (SOT), the X-Ray Telescope (XRT), and the EUV Imaging Spectrometer (EIS). EIS aboard Hinode is a high spectral resolution spectrometer aimed at studying dynamic phenomena in the corona (Culhane et al. 2007). EIS has two spectral ranges, 170–210 Å and 250–290 Å, which include emission lines from the transition region, the corona, and solar flares. EIS was designed to achieve high spatial resolution and sensitivity in order to study coronal activity in detail.

EIS successfully observed the 2006 December 13 flare with the JTM004 observing sequence. JTM004 contains nine spectral windows centered on Fe X (184.54 Å; $\log T/\mathrm{K} = 6.0$), Fe VIII (185.21 Å; $\log T/\mathrm{K} = 5.6$), Fe XI (188.23 Å; $\log T/\mathrm{K} = 6.1$), Ca XVII (192.82 Å; $\log T/\mathrm{K} = 6.7$), Fe XII (195.12 Å; $\log T/\mathrm{K} = 6.1$), Fe XIII (202.04 Å; $\log T/\mathrm{K} = 6.2$), He II (256.32 Å; $\log T/\mathrm{K} = 4.9$), Fe XIV (274.20 Å; $\log T/\mathrm{K} = 6.3$), and Fe XV (284.16 Å; $\log T/\mathrm{K} = 6.3$). Each raster consists of 512 slit positions, each with 30 s exposure duration, resulting in an effective cadence of ~ 4.5 hr. The slit, itself, is $1'' \times 256''$, yielding a $\sim 512'' \times 256''$ field of view. The sequence started from 01:12 UT and ended at 05:42 UT. Fortunately, the large X-class flare occurred during raster scanning. At 02:15 UT during the impulsive phase, we observed a flare arcade, which was located close to a sunspot around solar $X \sim 350''$ and solar $Y \sim -100''$. We calibrated the EIS data using the eis_prep routine in SolarSoft, which corrects for any flat field, dark current, cosmic rays, and hot pixels. An additional instrumental effect is a thermal one, in which there is an orbital variation of the line position, causing an artificial Doppler shift of $+/- 20 \, \mathrm{km\,s^{-1}}$, which follows a sinusoidal behavior. The orbital variation is well discussed in Brown et al. (2007). Our method of reducing the orbital variation effect is as follows: (1) we estimate the distribution of line center position along the slit in each raster step, (2) fit the distribution by a normal distribution function to estimate the most probable line center position in each raster step, and (3) the time profile of the line center position is obtained. By this statistical treatment, we reduce the instrumental effects to below $+/- 5 \, \mathrm{km\,s^{-1}}$.

Figures 1a–1c show He II, Fe XIV, and Fe XV intensity maps. The horizontal axis shows the raster step and the vertical axis shows the slit position. The raster step of this sequence is $\sim 0.''96$. Therefore, the vertical and horizontal axes roughly represent the X and Y directions in arcsec, respectively. The observation time is shown at the top of the figure. Note that EIS raster scanning starts from the West side (right hand side in figures 1a–1c) to the East side (left hand side in figures 1a–1c).
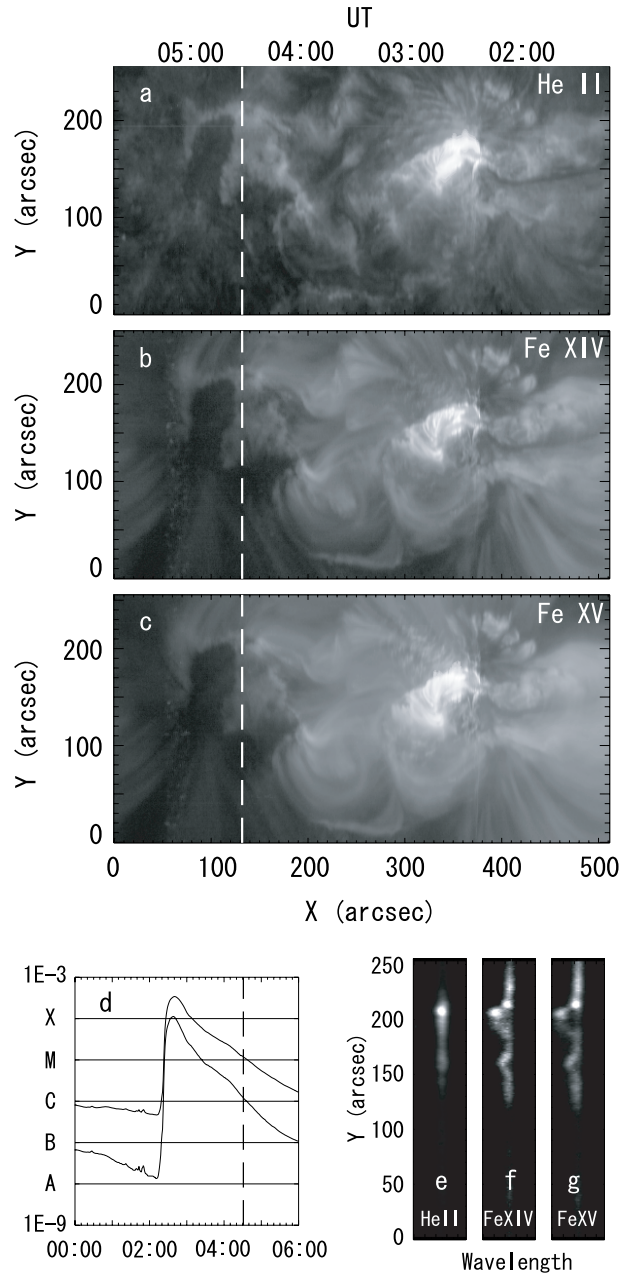
Fig. 1. EIS intensity maps for a range of He II, Fe XIV, and Fe XV (a)–(c). The gray scale shows the logarithm of the intensity. The flare arcade is located around $(X, Y) = (350, 150)$. GOES light curves of 1.0–8.0 Å and 0.5–4.0 Å are shown in (d). The impulsive phase starts around 2:10 UT. EIS CCD images for He II, Fe XIV, and Fe XV, are shown in (e)–(g). The horizontal axes in (e)–(g) show the wavelength, which ranges over 256.06–256.58, 273.96–274.47, 283.92–284.43 Å, respectively. The CCD images were acquired in the plage region, which is shown by the dashed white lines in (a)–(c). The acquired time is shown in (d) with a dashed line. The strong blue shifts were observed at $Y \sim 200$ in (f) and (g).

Therefore, the right-side images were taken before the left-side images (figures 1a–c). Figure 1d shows the light curve of GOES 1.0–8.0 and 0.5–4.0 Å. Figures 1e–1g show the He II, Fe XIV, and Fe XV CCD image of one slit position ($X \sim 132$). The white dashed lines in figures 1a–1c show the place where

the CCD images (figures 1e–1g), were taken in the intensity map. The dashed line in figure 1d shows the time when the CCD images were acquired.

In figures 1a–1c, we can clearly see flare arcades around $(X, Y) = (350, 150)$. We can also clearly see a region where the intensity is weaker than the usual corona in all three emission lines around the plage region, $(X, Y) \sim (100, 180)$. The CCD images were acquired during the gradual phase in the plage region, which was located $\sim 200''$ eastward from the flare arcade. We can clearly see strong blueshifts in the Fe XV and Fe XIV spectral lines in figures 1f and 1g around $Y \sim 200$. The interesting thing is that there is no strong blueshift in the He II line in figure 1e. The Fe XV emission line shows a stronger blueshift than that of the Fe XIV, although the temperature difference between them is small. Therefore, the blueshift is strongly dependent on the temperature. Note that EIS observed the plage region at $\sim 04{:}30$ UT. At that time it was located near the solar disk center, solar $X \sim 150$ and solar $Y \sim -100$.

We have studied the velocity maps in order to understand the temperature-dependent blueshifts. Figure 2a shows a velocity map of the Fe XV emission line. Figures 2b–2g show velocity maps of Fe XV, Fe XIV, Fe XIII, Fe XII, Fe X, and He II inside the white dashed box region of figure 2a. The color scale of these velocity maps are the same. They were obtained by a center-of-gravity method with an orbital variation correction.

In figure 2a, we can see redshifts at around the flare arcade. The downflow in the flare arcade is also interesting, but in this paper we concentrate on the upflow of the plage region. A detailed study of downflow in the flare arcade will be reported elsewhere. We can clearly see strong blueshifts in the plage region, in Fe XV ($T_{\mathrm{e}} = 2.1\,\mathrm{MK}$) in figure 2a, at the boundary of a weak intensity region. The strong blueshifts are concentrated on $(X, Y) \sim (130, 200)$ or $\sim (170, 140)$ in figure 2a. The strongest blueshifts are greater than $100\,\mathrm{km\,s^{-1}}$. Fe XIV ($T_{\mathrm{e}} = 1.8\,\mathrm{MK}$) and Fe XIII ($T_{\mathrm{e}} = 1.6\,\mathrm{MK}$) also show strong upward flow at the boundary of a weak intensity region in figures 2c and 2d. On the other hand, Fe XII ($T_{\mathrm{e}} = 1.4\,\mathrm{MK}$) and Fe X ($T_{\mathrm{e}} = 0.98\,\mathrm{MK}$) show weaker blueshifts in figures 2e and 2f. Furthermore, in He II ($T_{\mathrm{e}} = 0.087\,\mathrm{MK}$) there are no longer clear blueshifts. Comparing the magnitude of the velocity for these emission lines (figures 2b–2g), we can see that these upflows clearly depend on the temperature. Another interesting thing is the duration of this continuous upflow. This plage upflow seems to be associated with a X class flare. We checked a December 12 velocity map to confirm that there was no such high velocity upflow (not shown here). The X-class flare took place at $\sim 02{:}00$ UT, and EIS observed the plage region at $\sim 04{:}30$ UT. Therefore, these upflows continue for longer than two hours.

From figure 2, we find the dependence between upflow and temperature. To clarify this dependence from an observational point of view, we considered a line spectrum with double Gaussian fitting. Figures 3a–3f show the spectra taken from corona high-temperature emission lines (Fe XV, Fe XIV, Fe XIII). The horizontal and vertical axes show the wavelength and intensity, respectively. Figures 3a–3c show a reference spectrum with a single Gaussian fitting to define the line center, which is emitted from a stationary component. These reference lines were taken at $(X, Y) = (132, 231)$, which is just outside
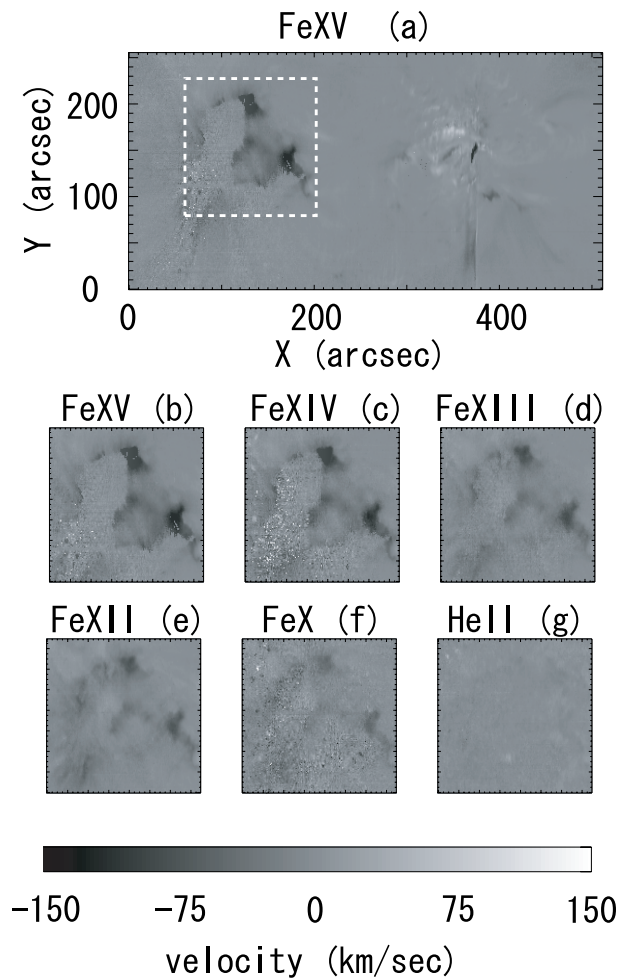

Fig. 2. EIS velocity map, $512'' \times 256''$, for Fe XV (a). The EIS velocity maps for a range of Fe XV, Fe XIV, Fe XIII, Fe XII, Fe X, and He II in the plage region, which is shown by a white dashed box in (a). The color scale is the same for all figures. The velocity map of the highest temperature line, Fe XV, shows strong blueshifts. On the other hand, other lower temperature lines, Fe XII, Fe X, show weak blueshifts. There are no clear blueshifts in the He II line.

of the white dashed box in figure 2a. The dashed lines in figure 3 represent the line center, which is emitted from the stationary component. Figures 3d–3f show a blueshift spectra with a double-Gaussian fitting at $(X, Y) = (132, 206)$. The solid line shows the result of a two-component Gaussian fitting. The dashed and dotted lines show the blueshift and stationary components, respectively. The method of double-Gaussian fitting used was as follows: we defined each line center using the reference spectrum, and then fit the blueshift spectrum with the stationary and blueshift components. This method is the same as that of Milligan et al. (2006).

We can clearly see two peaks in the Fe XV spectrum. The intensity of the blueshift component is three-times as much as that of stationary component. This indicates that there are two emission sources in the Fe XV temperature, and the major source shows the strong blueshift. The difference in wavelengths between the blueshift and the stationary component is $0.154\,\text{Å}$, which corresponds to $160\,\mathrm{km\,s^{-1}}$ in
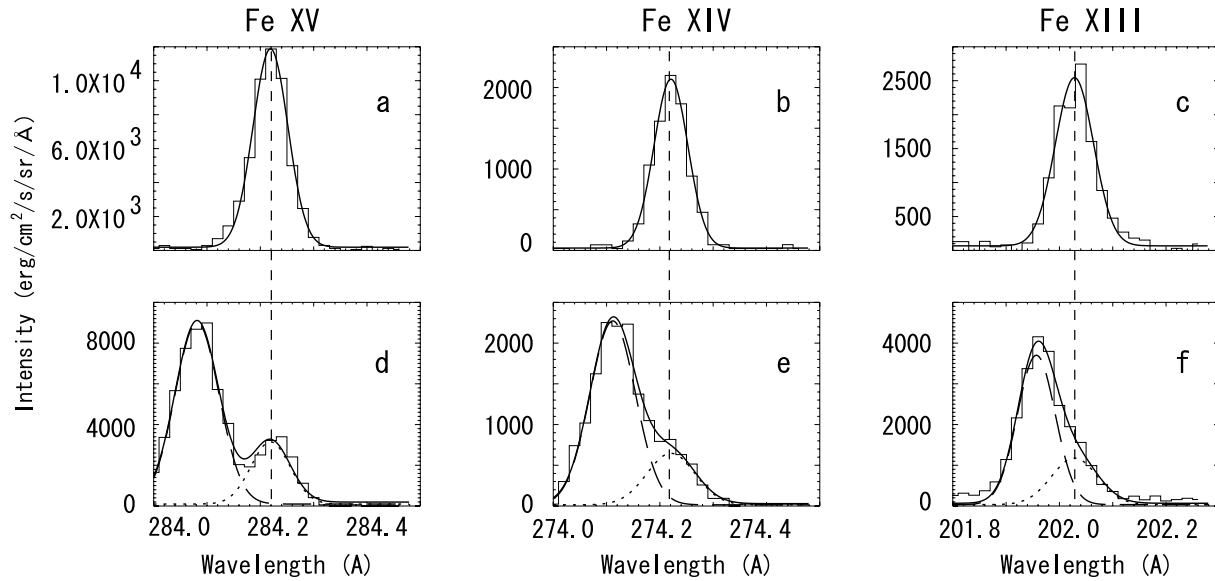
Fig. 3. Sample of spectra taken from corona high-temperature emission lines (Fe XV, Fe XIV, Fe XIII). The vertical axes show the intensity, and the horizontal axes show the wavelength. The vertical dashed lines show the line center of the emission lines, which are emitted from stationary ions. The upper panels show reference emission lines, which seem to be emitted from a stationary plasma, to determine the line center, (a)–(c); the lower panels show the emission lines of the plage region, which exhibit strong blueshifts.
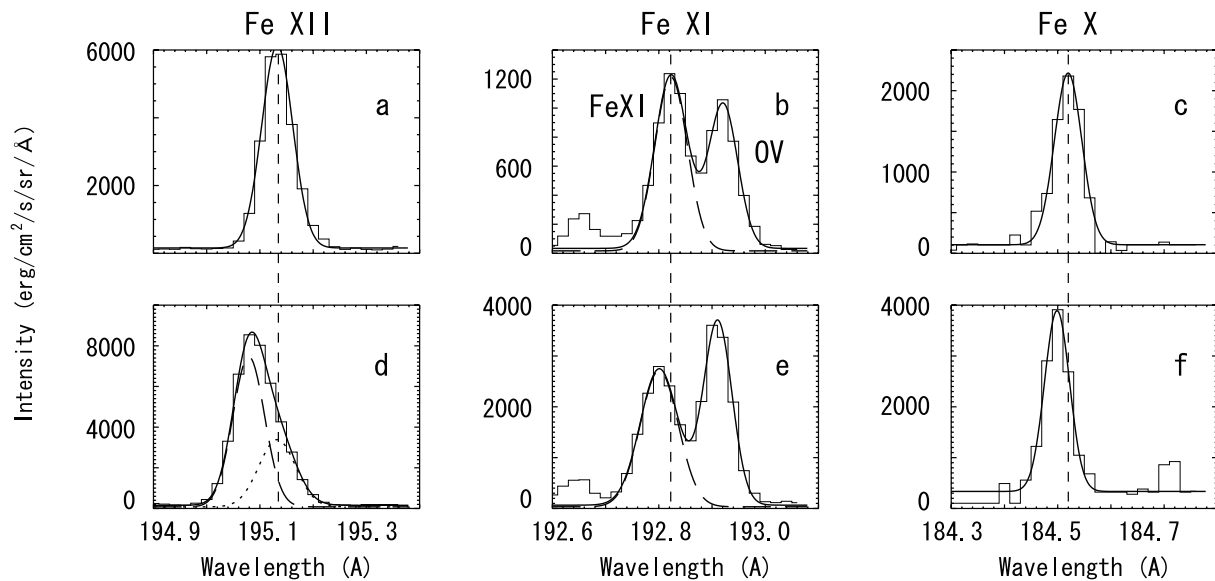
Fig. 4. Sample of spectra taken from corona middle temperature emission lines (Fe XII, Fe XI, Fe X). The figure format is the same as in figure 3.

velocity. In Fe XIV and Fe XIII (figures 3e and 3f), we can also observe two components. The differences in wavelengths between the blueshift and stationary components in Fe XIV and Fe XIII are 0.122 Å and 0.080 Å, which correspond to 130 and 120 km s^{-1}, respectively.

Figures 4a–4f show the spectra taken from the mid-temperature corona (i.e., Fe XII, Fe XI, Fe X). The figure format is the same as in figure 3. In this temperature range, it is very hard to distinguish between the stationary and blueshifted components, because the blueshift is weaker than that of the high-temperature corona lines. Therefore, we fit

only the Fe XII spectrum with a double Gaussian and Fe XI; Fe X were fitted with a single Gaussian. We could estimate the blueshift by the difference between the reference spectrum, figures 4b and 4c, and the blueshift spectrum, figures 4e and 4f. Note that there are two peaks of emission lines in figures 4b and 4e. The left peak represents Fe XI emission line and the other represents the O V line. This spectral window (192.56–193.07 Å) includes the Ca XVII emission line ($\log T/\mathrm{K} = 6.7$), which is one of the EIS core lines. In this case, the electron temperature is not high enough for Ca XVII to be observed, allowing us to clearly see the Fe XI and O V lines
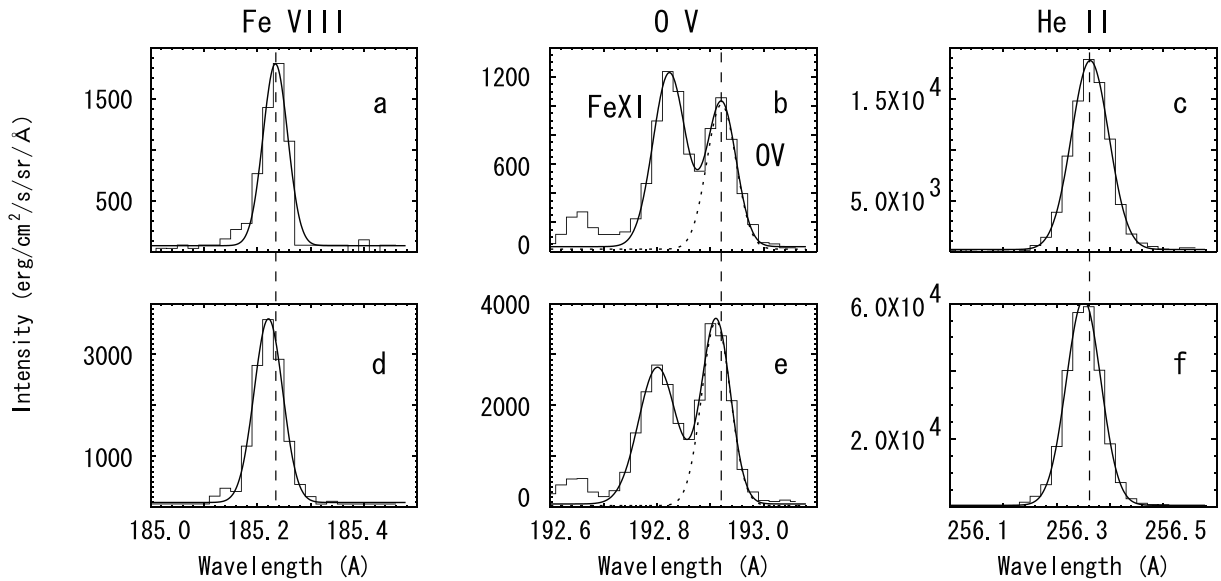
Fig. 5. Sample of spectra taken from corona low-temperature emission lines (Fe VIII, O V, He II). The figure format is the same as in figure 3.

in this window. The differences of the wavelength between the blueshifted and stationary components in Fe XII, Fe XI, and Fe X are 0.060, 0.025, and 0.023 Å, which correspond to 90, 40, and 35 km s^{-1}, respectively.

Figures 5a–5f show the spectra taken from the corona/transition region low-temperature emission lines (Fe VIII, O V, He II). The figure format is also the same as in figure 3. The O V line is in the same line window of Fe XI that is mentioned above. At this temperature, we can no longer distinguish between the stationary and blueshift components. The differences in the wavelength between the blueshift and reference lines in Fe VIII, O V, and He II are 0.015, 0.011, and 0.012 Å, which correspond to 23, 18, and 16 km s^{-1}, respectively. These results confirm that the upflow velocity is strongly dependent on the temperature.

Figure 6 shows the upflow velocity as a function of temperature with the dashed line showing the sound speed. The line formation temperatures are defined by the temperature that yields its peak abundance with the CHIANTI code (Landi et al. 2006). Note that the orbital variation effect is not included in this result. All of the spectra in figures 3–5 were obtained by the same raster position. This means that they were obtained simultaneously. The errors should be estimated by the double value of the EIS wavelength precisions at the 2 sigma level, $+/-0.1$ pixel (Brown et al. 2007), because we obtained figure 6 using two spectrum images. Thus, the velocity errors were estimated by $+/-$ a quarter of the EIS spectral resolution. Below 1 MK, the upflow velocities weakly depend on the temperature. However, the trend of the dependence changes dramatically above 1 MK, and the upflow velocity is up to sound speed. From the view point of Mach number, we can clearly see that the Mach number decreases with temperature in the low-temperature range, and increases in the high-temperature range in figure 6. Although we assume that the temperature of each emission line is the peak of the contribution function, there is clearly a relationship between
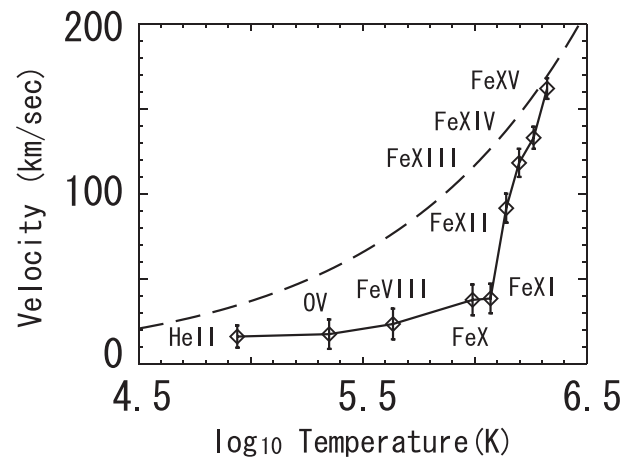

Fig. 6. Upflow velocity as a function of the temperature. The dashed line shows the sound speed. Around 1 (MK), the trend of the temperature dependence is significantly changed. The upward velocity is almost the sound speed in Fe XV.

the upflow velocity and the temperature, and this dependence dramatically changed around 1 MK. There are a number of studies that discuss the variation of the Doppler shift or line width with temperature in both the quiet Sun and the active region (e.g. Peter & Judge 1999; Hara & Ichimoto 1999). Some of these results also show that there is a turning point at 0.5–1 MK.

3. Discussion and Summary

We studied the characteristics of upflows in the plage region during the gradual phase of an X-class flare. We found the following: (1) the strong blueshifts associated with the flare were observed in the plage region, (2) these upflows were dependent on the temperature, (3) the duration time
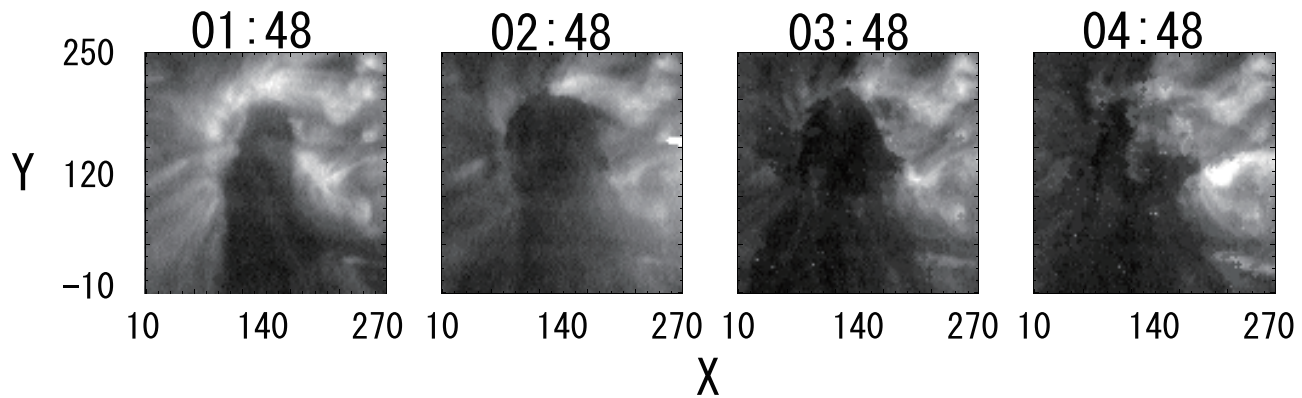
Fig. 7. Time evolution of the plage region observed by SoHO/EIT 195 Å. The color scale is the same in all images. A pre-flare image is shown in the left figure (01:48 UT). From the center-left to the right image (02:48–04:48 UT), a transient coronal hole shows some dynamical changing. The units of the horizontal and vertical axes are the same as in figure 1.

of the upflows was longer than two hours, (4) the trend of the upflow dependence on temperature dramatically changed at around 1 MK.

Let us discuss the time evolution of the plage region. Figure 7 shows the time evolution of the plage region observed by SoHO/EIT (195 Å) with one hour cadence. The color scales of these figures are the same. The left figure, 01:48 UT, shows a pre-flare image of the plage region. In the center of the figure, we can already see the weak intensity region. We checked the intensity map of December 12 and found that the weak intensity region is not a short-lived one. It looks similar to a coronal hole, but its spatial size is not as large as the usual coronal hole. The intensity of the weak intensity region is slightly below that of the usual quiet region, but it is higher than that of the coronal hole (not shown here). Another characteristic that should be mentioned is that the region dominantly has positive magnetic fields. At the pre-flare stage, it is plausible that there were no strong blueshifts from the plage region, because there was no strong blueshift on the December 12 velocity map, as we mention above. The center-left figure, 02:48 UT, shows the image of a transient coronal hole just after the flare. If we look carefully, we can find that the intensity of the transient coronal hole boundary become weaker than that at the pre-flare time. This result is one piece of evidence that there are some interactions between the transient coronal hole and an X-class flare. It is plausible that some parts of closed loops interact with the open magnetic fields, and plasma escapes along the open field lines. Actually, fast solar winds of up to $1000\,\mathrm{km\,s^{-1}}$ and CME were observed by ACE, which flies near to Earth. At the post-flare stage in the center-right and right figures, 03:48 UT and 04:48 UT, we can see some recovery feature, especially on the right side of the transient coronal hole. We can clearly see that some bright structures penetrate into the center of the transient coronal hole. We think that these dynamical features were caused by a changing magnetic topology. In general, the dynamical time scales are defined by the ratio of the Alfvén velocity and the scale size, which is roughly 100 seconds in the coronal active region. However, the EIT observation indicates a rather long timescale. A changing dynamical topology associated

with a flare is intensively discussed in Attrill et al. (2006) and Harra et al. (2007), in the context of CME formation. According to their study, a dimming associated with topology changes occurs rapidly, although the recovering intensity of the dimmed regions appears to be a relatively steady. This result may indicate that the changing topology at the dimming stage occurs at one time, although the changing at the recovering stage occurs step by step.

One of the most interesting findings in our study is that the upflows in the plage region sensitively depend on the temperature. In the context of solar-wind formation, one of the most important things is coronal heating. Solar-wind formation with coronal heating has been intensively discussed by many people (e.g., Cranmer et al. 2002; Suzuki & Inutsuka 2005). Our new findings may suggest that heating has an important role for solar-wind formation. Especially, we think that coronal heating at around 1 MK is the key to the understanding solar-wind formation, because the trend of the upflow dependence on temperature is dramatically changed. We are now starting a detailed analysis of the temperature-dependent upflow with a 1D steady state assumption. From our preliminary result of 1D steady state analysis, there are strong heating sources at a height of ∼ 50 Mm. These results will be discussed elsewhere.

References

Attrill, G., Nakwacki, M. S., Harra, L. K., van Driel-Gesztelyi, L., Mandrini, C. H., Dasso, S., & Wang, J. 2006, Sol. Phys., 238,117

Brown, C. M., et al. 2007, PASJ, 59, S865

Chen, P. F., & Shibata, K. 2000, ApJ, 545, 524

Cranmer, S. R. 2002, Space Sci. Rev., 101, 229

Crooker, N. U., Gosling, J. T., & Kahler, S. W. 2002, J. Geophys. Res., 107, SSH3–1

Culhane, J. L., et al. 2007, Sol. Phys., 243, 19

Hara, H., & Ichimoto, K. 1999, ApJ, 513, 969

Harra, L. K., Hara, H., Imada, S., Young, P. R., Williams, D. W., Sterling, A. C., Korendyke, C., & Attrill, G. D. R. 2007, PASJ, 59, S801

Kosugi, T., et al. 2007, Sol. Phys., 243, 3

Landi, E., Del Zanna, G., Young, P. R., Dere, K. P., Mason, H. E., & Landini, M. 2006, ApJS, 162, 261

Masuda, S., Kosugi, T., Hara, H., Tsuneta, S., & Ogawara, Y. 1994, Nature, 371, 495

Milligan, R. O., Gallagher, P. T., Mathioudakis, M., Bloomfield, D. S., Keenan, F. P., & Schwartz, R. A. 2006, ApJ, 638, L117

Ohyama, M., & Shibata, K. 1998, ApJ, 499, 934

Peter, H., & Judge, P. G. 1999, ApJ, 522, 1148

Suzuki, T. K., & Inutsuka, S. 2005, ApJ, 632, L49

Teriaca, L., Falchi, A., Cauzzi, G., Falciani, R., Smaldone, L. A., & Andretta, V. 2003, ApJ, 588, 596

Tsuneta, S., Hara, H., Shimizu, T., Acton, L. W., Strong, K. T., Hudson, H. S., & Ogawara, Y. 1992, PASJ, 44, L63

Yokoyama, T., Akita, K., Morimoto, T., Inoue, K., & Newmark, J. 2001, ApJ, 546, L69